

## Simulation of thermal cycle aging process on fiber-reinforced polymers by extended finite element method

González, Sergio; Laera, Gianluca; Koussios, Sotiris; Domínguez, Jaime; Lasagni, Fernando A.

**DOI**

[10.1177/0021998317734625](https://doi.org/10.1177/0021998317734625)

**Publication date**

2018

**Document Version**

Final published version

**Published in**

Journal of Composite Materials

**Citation (APA)**

González, S., Laera, G., Koussios, S., Domínguez, J., & Lasagni, F. A. (2018). Simulation of thermal cycle aging process on fiber-reinforced polymers by extended finite element method. *Journal of Composite Materials*, 52(14), 1947-1958. <https://doi.org/10.1177/0021998317734625>

**Important note**

To cite this publication, please use the final published version (if applicable). Please check the document version above.

**Copyright**

Other than for strictly personal use, it is not permitted to download, forward or distribute the text or part of it, without the consent of the author(s) and/or copyright holder(s), unless the work is under an open content license such as Creative Commons.

**Takedown policy**

Please contact us and provide details if you believe this document breaches copyrights. We will remove access to the work immediately and investigate your claim.

# Simulation of thermal cycle aging process on fiber-reinforced polymers by extended finite element method

Sergio González<sup>1</sup>, Gianluca Laera<sup>1</sup>, Sotiris Koussios<sup>2</sup>, Jaime Domínguez<sup>3</sup> and Fernando A Lasagni<sup>1,3</sup>

## Abstract

The simulation of long life behavior and environmental aging effects on composite materials are subjects of investigation for future aerospace applications (i.e. supersonic commercial aircrafts). Temperature variation in addition to matrix oxidation involves material degradation and loss of mechanical properties. Crack initiation and growth is the main damage mechanism. In this paper, an extended finite element analysis is proposed to simulate damage on carbon fiber reinforced polymer as a consequence of thermal fatigue between  $-50^{\circ}\text{C}$  and  $150^{\circ}\text{C}$  under atmospheres with different oxygen content. The interphase effect on the degradation process is analyzed at a microscale level. Finally, results are correlated with the experimental data in terms of material stiffness and, hence, the most suitable model parameters are selected.

## Keywords

Thermal aging simulation, finite element method, composite materials, carbon fiber reinforced polymer, long life behavior

## Introduction

Owing to the growing use of composite materials at different sectors, and more complexity of structural designs,<sup>1</sup> mechanical models are increasingly required nowadays for the simulation of components.<sup>2</sup> Static and fatigue properties as well as damage mechanisms have been intensely studied for the last three decades.<sup>3</sup> On the other hand, environmental aging of carbon fiber reinforced polymers (CFRPs) (i.e. thermal fatigue effects) is still under investigation.<sup>4–9</sup> In this context, one of the main damage mechanisms is the material cracking caused by thermal cycles.<sup>10–12</sup> The studies,<sup>13,14</sup> which analyze the influence of oxidative environment on the damage development, suggest that a coupled mechanism exists between: (i) the epoxy matrix oxidation at high temperatures, and (ii) thermal fatigue due to different coefficients of thermal expansion (CTE) within the composite system.

Several kinetic models have been proposed in order to estimate the matrix oxidation process and its effect.<sup>15,16</sup> Its main consequence is the variation of the Young's modulus ( $E$ ) with the exposure time.<sup>17</sup>

At a microscale level, three regions with different properties may be considered in a composite material:

fiber, matrix, and interphase. The latter is produced by the chemical reaction between matrix and fiber during the curing process.<sup>18,19</sup>

Asp et al.<sup>20,21</sup> performed a static parametric finite element analysis of a unit cell to determine the relation between the interphase properties and the transverse strength of the material. Three different types of interphases were studied: rubbery, thermoplastic, and medium elastic modulus. Each of them associated with three relative thicknesses of the layer (1%, 5%, and 10% of the fiber diameter). It was found that the interphase properties have a decisive influence on the location and the mode of failure, whereas Poisson's

<sup>1</sup>Advanced Center for Aerospace Technologies – CATEC, Spain

<sup>2</sup>Department of Structural Integrity & Composites, Delft University of Technology, The Netherlands

<sup>3</sup>Department of Materials & Mechanical Engineering, University of Seville, Spain

## Corresponding author:

Sergio González, Advanced Center for Aerospace Technologies – CATEC, Wilbur y Orville Wright, 17-19-21, 41309 La Rinconada-Seville, Spain.

Email: [sgonzalez@catec.aero](mailto:sgonzalez@catec.aero)

ratio is not a critical parameter for the prediction of damage initiation.

Tanoglu et al.<sup>22,23</sup> used a specifically designed testing machine (dynamic interphase-loading apparatus) to characterize the interphase mechanical behavior of a glass–epoxy system. They demonstrated that the shear strength and the energy absorption characteristics of the interphase strongly affect the performance of the composite, concluding that a low value of the first property considerably enhances the last one.

In this paper, crack initiation and growth, as a consequence of thermal fatigue degradation, are numerically analyzed at a microscopic level, where the effect of the interphase between fiber and epoxy matrix is appreciable.<sup>24,25</sup> The results are then compared with the experimental data from the tests performed on samples exposed to the same conditions as simulated in this study.

As it is a microscopic model, a representative unit cell of the real problem must be selected. In composite materials, the arrangement of fibers is usually random within a layer. However, for the purpose of this study, two main idealizations may be considered: square and hexagonal packing.<sup>26</sup> A random distribution of fibers in a plane perpendicular to the fiber direction results in transverse (statistical) isotropy. The same property can be achieved with a hexagonal packing, but not with a square one.<sup>27</sup> The property of transverse isotropy is fundamental when applying boundary conditions in a case of thermal loading, thus hexagonal packing will be used in this paper.

The organization of the paper is as follows. First, material properties and experiments are described. Then the computational model is defined and the analysis is performed. Subsequently, numerical results are presented and compared with the experimental results. Finally, conclusions are provided and future developments are established.

## Materials and experiments

The material analyzed in this investigation is a carbon fiber/epoxy composite. The resin used is Hexply<sup>®</sup> 8552 (amine cured, toughened epoxy system) and the fiber is a HexTow<sup>®</sup> AS4 (continuous high strength, high strain PAN-based carbon fiber). The fiber volume ( $V_f$ ) in this case is 58%. The constituent mechanical properties at 20°C, and referred to transversal direction, are shown in Table 1.

The fiber properties are considered constant with temperature in the selected range (−50°C/+150°C). Young's modulus and CTE of the matrix vary with temperature according to the equations proposed by Zhang<sup>28</sup> for an epoxy resin (equations (1) to (3)),

**Table 1.** Properties of the materials at 20°C (transversal direction).

Property (20°C)	Resin	Fiber
Young's modulus, $E$ (GPa)	4.67	20
CTE (m/m·K)	$58 \times 10^{-6}$	$18 \times 10^{-6}$
Conductivity (W/m·K)	0.15	2.4
Tensile strength, $\sigma_u$ (MPa)	120	–
Shear strength, $\tau_u$ (MPa)	80	–
$\nu$	0.37	0.2
$G_{IC}$ (J/m <sup>2</sup> )	679	–
$G_{IIC}$ (J/m <sup>2</sup> )	1100	–

where  $T_r$  is the room temperature and  $T_g$  is the glass transition temperature.

$$E(T) = E(T_r) \exp\left(-k_1 \frac{T - T_r}{T_g - \Delta T - T_r}\right) \quad (1)$$

With:  $E(T_r) = 4.67$  GPa;  $T_g = 180^\circ\text{C}$ ;  $\Delta T = 30^\circ\text{C}$ ;  $T_r = 20^\circ\text{C}$ ;  $k_1 = 0.35667$

$$CTE(T) = K(T - T_r) + CTE(T_r) \quad (2)$$

$$K = \frac{CTE_1 - CTE(T_r)}{T_g - T_r} \quad (3)$$

With:  $CTE(T_r) = 58 \times 10^{-6} \text{ m}\cdot(\text{m}\cdot\text{K})^{-1}$ ;  $CTE_1 = 139 \times 10^{-6} \text{ m}\cdot(\text{m}\cdot\text{K})^{-1}$

The rest of the matrix mechanical properties are considered constant with the temperature.

During the experimental investigation, 500 thermal cycles between −50°C and 150°C, at 15°C/min and 5 min dwell time were applied on CFRP samples. Cycles were performed by means of the test chamber Angelantoni-ACS UHS1400 (Figure 1(a)). Figure 1(b) shows the specifically designed system for the control of the atmosphere composition.

Two different sizes of samples— $25 \times 35 \text{ mm}^2$  and  $180 \times 18 \text{ mm}^2$ —were used in light optical microscopy (LOM) and static tensile tests, respectively (Figure 1(c)). The selected material was also AS4/8552 prepreg with a  $[0_3/90_3]_s$  stacking sequence and nominal thickness of 2.21 mm. Applied curing conditions were 3 h long cycle at 180°C, with a 7 bar pressure.

The thermal cycling test was performed applying two different atmospheres. The first one represented a neutral atmosphere (nitrogen gas) for isolating any effect of oxidative agents. This condition was referred to as inert. Dry air was used for the second atmosphere to introduce effects related to material oxidation. It was referred to as oxidative condition and applied in the

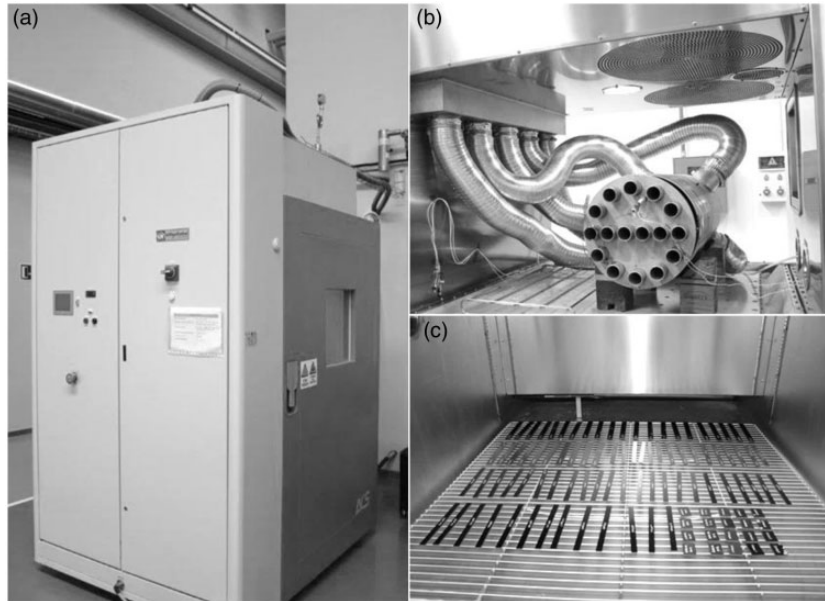


**Figure 1.** (a) Environmental test chamber for thermal cycling tests, (b) controlled atmosphere system, and (c) samples for experimental analysis.

same temperature range as for the neutral atmosphere. Matrix oxidation was expected at high temperatures, while matrix cracking occurred due to the mismatch of thermal expansion coefficient. Coupling of both effects produced the aging acceleration of CFRP.

Finally, loss of the mechanical properties was analyzed by the comparison of Young's modulus variation between simulation and experimental tensile tests, before and after environmental aging. The equipment used for the mechanical quasi-static tests was the universal testing machine Zwick Z100. Tests were performed with a force control, applying a test speed of 2 mm/min until the failure of the specimens was reached. Young's modulus was evaluated by means of a calibrated extensometer.

### Computational analysis

The study was performed by modifying two parameters: Young's modulus ( $E$ ) and interphase thickness ( $t$ ). Three interphase thicknesses were used for the parametric analysis: 1%, 2.5%, and 5% of the fiber radius ( $3.5\ \mu\text{m}$ ), each one related to three different elastic modulus. Values of 12 GPa and 6 GPa represent interphases with 60% and 30% of the transversal stiffness of the fiber, respectively, whereas modulus of 0.01 GPa represents a rubbery interphase. Poisson's ratio and CTE were estimated to be equal to that of the matrix. However, the interphase strength was established as a percentage of the resin values in order to consider microscopic imperfections that affect matrix and fiber bonding. Tensile and shear strength values were

80 MPa and 25 MPa, respectively. Therefore, the whole investigation consisted of 27 case studies, considering different simulations of the initiation and fatigue steps.

Since the selected unit cell (Figure 2(a)) shows two directions of reflection symmetry, just a quarter of it is analyzed (Figure 2(b)), imposing symmetry conditions on the initiation step, where no crack propagation is expected inside the matrix. However, in the case of the fatigue steps, the complete cell was considered (Figure 2(c)) to allow a wider range of possibilities for the crack path simulations (i.e. cracks initiated in a quarter of the cell growing to an adjacent one).

Loads and boundary conditions must be representative of a thermal fatigue problem. As shown in Figure 3, for both crack initiation and fatigue steps, the displacement in the  $x$ -direction is not allowed for the nodes located at the left-edge (P-S), and the displacement in the  $y$ -direction is not allowed for the bottom edge (P-Q). The right (Q-R) and top (R-S) edges remain parallel respectively, to the left and bottom ones in order to guarantee the periodicity of the cell. The displacement values, imposed at the top and right edge of the model, depend on the fiber volume fraction, length of each edge, and applied temperature.<sup>29</sup>

The element selected for this analysis is a 4-node bilinear plane strain quadrilateral with a reduced integration (CPE4R in Abaqus® software). After the convergence analysis, modifying the number of the elements used, the average element size was  $1.73 \times 10^{-2}\ \mu\text{m}$ . Larger elements were used for the fiber part, where no damage is expected.

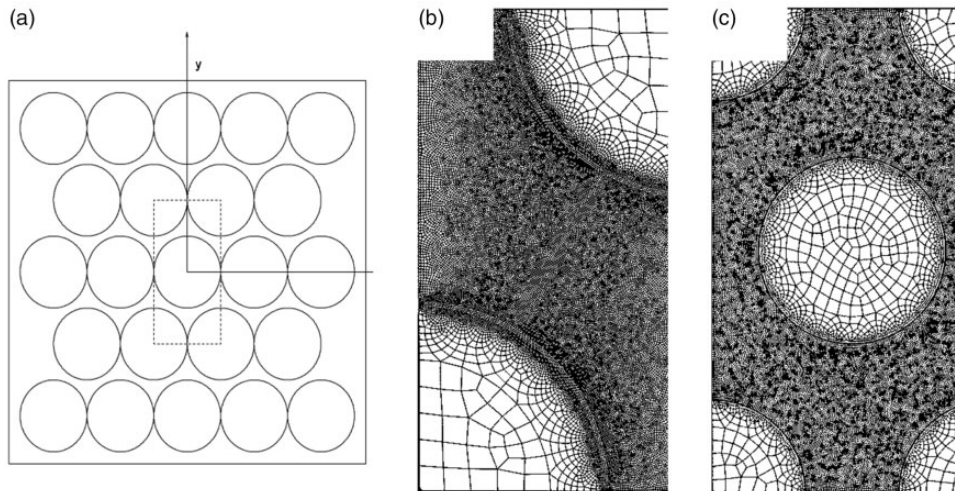


**Figure 2.** (a) Unit cell configuration considered for the thermal fatigue problem, (b) mesh used for crack initiation, and (c) meshing for thermal fatigue steps (inert and oxidative).

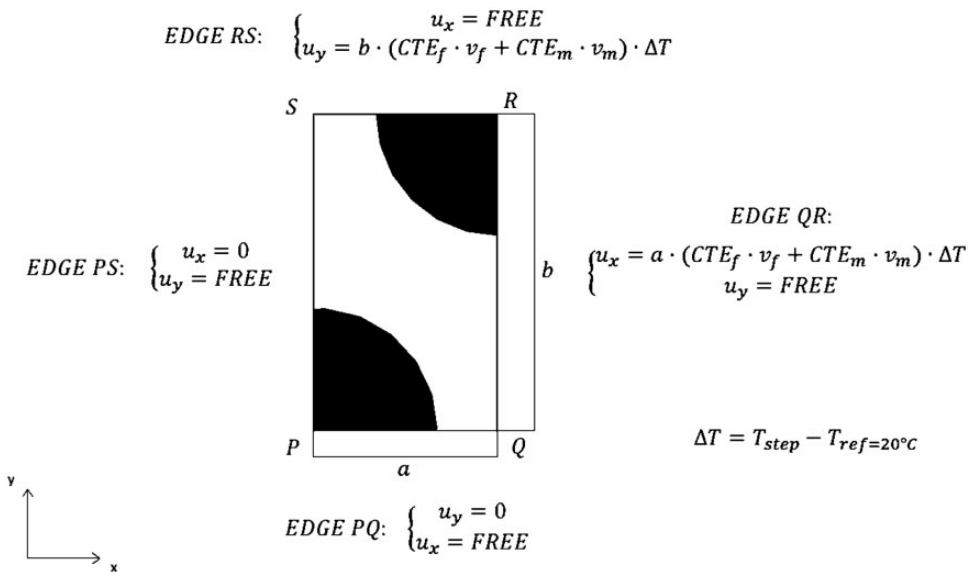


**Figure 3.** Boundary conditions applied.

The X-FEM analysis was structured in three different steps as described in the following.

**Damage initiation step**

It is a static analysis, applying one thermal cycle to study how the model parameters affect the crack nucleation process. The results are evaluated by means of two variables: one related to the size of the crack through a damage ratio parameter ( $\beta$ ), calculated as the ratio between the number of damaged elements and the number of elements at the interphase; and the second with the initiation temperature (temperature at

which first cracked element appears). The latter is evaluated as the temperature increment, when the stress field perturbation is detected in any of the two paths, as shown in Figure 4. The paths are concentric with the separation line between the matrix and the interphase. The separation distance depends on the parametric case, being selected as  $\pm 0.06 \mu m$  for the 2.5% and 5% cases, and  $\pm 0.015 \mu m$  for the 1% case.

In this initiation step, a cohesive approach was used to simulate the crack behavior. The quadratic nominal stress criterion, for two-dimensional problems, was selected for crack initiation (equation (4)), and a linear traction-separation law (defined through fracture

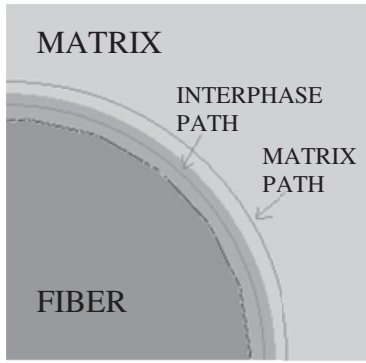


**Figure 4.** Matrix and interphase paths for temperature of damage initiation evaluation.

energy) is proposed for damage evolution within the step<sup>30</sup>

$$f = \left\{ \frac{\langle t_n \rangle}{t_n^0} \right\}^2 + \left\{ \frac{t_s}{t_s^0} \right\}^2 \quad (4)$$

where the nominal traction stress vector  $t$  consists of two components (three in 3D problems):  $t_n$  is the component normal to the likely cracked surface, and  $t_s$  is the in-plane shear component on the likely cracked surface.  $t_n^0$  and  $t_s^0$  represent peak values of the nominal stresses. Crack opening modes I and II are simulated in this study. Damage is assumed to initiate when the function defined in the above expression reaches a value of 1. The law of damage evolution and the traction-separation behavior describe the rate at which the cohesive stiffness is degraded.

### Inert fatigue step

For the fatigue analysis, up to 500 thermal cycles are simulated, or interrupted when the stabilization criteria is reached. In this study, the stabilization is considered when the model evolution (in terms of von Mises stresses) becomes stable and no changes occur in the stress field. Those changes are monitored by a control or representative element, which is lying on the straight line, connecting the center of two contiguous fibers at a distance of 0.2  $\mu\text{m}$  from the interphase–matrix separation line (Figure 5).

At the end of the analysis, the loss of the cell stiffness is related to the number of cracks by means of an equivalent displacement parameter. It is calculated by using the displacements at nodes of non-fixed edges

$$\delta u_{eq} = \sqrt{\delta u_x^2 + \delta u_y^2} \quad (5)$$

$\delta u_x$  evaluates the displacement of the edge RS, and  $\delta u_y$  is the displacement of the edge QR (as defined in

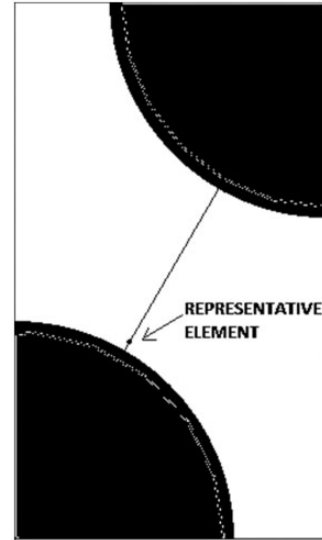


**Figure 5.** Element in which the von Mises stress at maximum temperature is evaluated in the fatigue analyses.

Figure 3) at the increment of maximum temperature of the last cycle. The equivalent displacement parameter is given as an indication of the cell degradation.

In the fatigue steps, simulation of the cracks is performed using the X-FEM procedure, evaluating the critical equivalent fracture energy release rate  $G_{eq,c}$  through the Benzeggagh–Kenane relation.<sup>31</sup> Crack growth is characterized by means of Paris law (equation (6)), using enriched elements with a propagating direction normal to the direction of the maximum tangential stress (MTS)

$$\frac{da}{dN} = c_3 \Delta G^{c_4} \quad (6)$$

where constants  $c_3$  and  $c_4$  are taken to be  $1 \times 10^{-8}$  and 2.5, respectively.<sup>32</sup>  $G_{thresh}$  and  $G_{pl}$  were selected as 1% and 85% of  $G_{eq,c}$ .

### Oxidation fatigue step

This analysis is similar to the inert one, but includes the oxidative effect as a variation on the matrix Young's modulus. This variation is calculated using the following<sup>33</sup>

$$E(t) = 5479 - 1460 \cdot e^{-5.859 \cdot 10^{-6} t} \quad (7)$$

In this study, the effect of the exposure time was evaluated considering the investigation performed by Lafarie-Frenot et al.<sup>34</sup> in 2006, who found that 500 h of isothermal aging of an epoxy resin may be equivalent to 500 thermal cycles in terms of weight reduction.

Equation (7) is valid for the Cytec<sup>®</sup> 977-2 resin. In order to adapt it to the resin used in this analysis, the following procedure was implemented. First,  $E(t)$  of the oxidized 977-2 resin was calculated at each cycle time; the value of  $E$  at  $t=0$  ( $E_{ref}$ ) was then subtracted from the oxidized 977-2 modulus, obtaining the difference, for each cycle, between the oxidized and nonoxidized resin modulus. This difference (in terms of percentage) was then used to modify, cycle by cycle, the unoxidized  $E_{ref}$  value of the 8552 resin, obtaining, for each value of time, the oxidized 8552 resin modulus at 20°C (keeping the same temperature dependency).

For the purpose of the oxidation analysis, the 500 thermal cycles were subdivided into 10 blocks of 50 cycles each. The value of  $E$  was calculated for the first cycle of each block, and kept constant for the following 49 cycles. Therefore, the elastic modulus is dependent on temperature and time (step) [ $E=f(T, \text{step})$ ]. The division in blocks is essential for decreasing the computational cost of analysis, which would have become prohibitive in case of indexing the elastic modulus with respect to each cycle.

Finally, the stiffness variation of every unit cell (from each model considered) is calculated as a percentage between the original cell and the aged one. This variation is compared with the reduction of the material's Young's modulus through the experimental tests.

## Results

According to the microscopy experiments carried out on different samples, the cracks start to develop within the first five cycles. Therefore, since oxidation is not relevant at this step of the process, damage initiation during the first static cycle is thought to approximate well with the real behavior of the material. Additionally, simulated cracks must grow from fiber to fiber, always surrounding them and not breaking, as is observed experimentally in the samples exposed to the thermal cycling (Figure 6).

From the damage initiation step, as noticeable in Figure 7, the role of the interphase is determinant. Soft, rubbery interphase avoids cracks, thus no

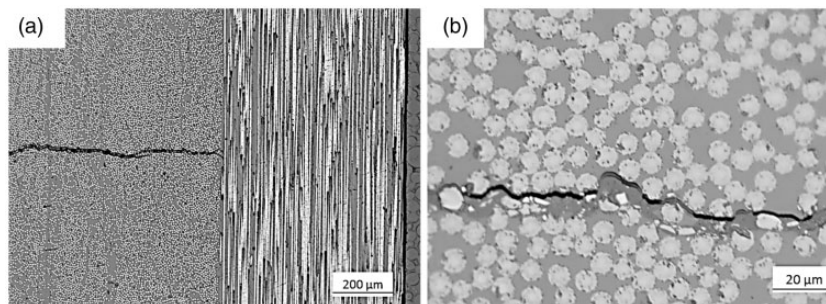


**Figure 6.** (a) 10× and (b) 100× microscopy results of a sample exposed to 200 thermal cycles under oxidative conditions. Dry air: 150°C/−50°C.

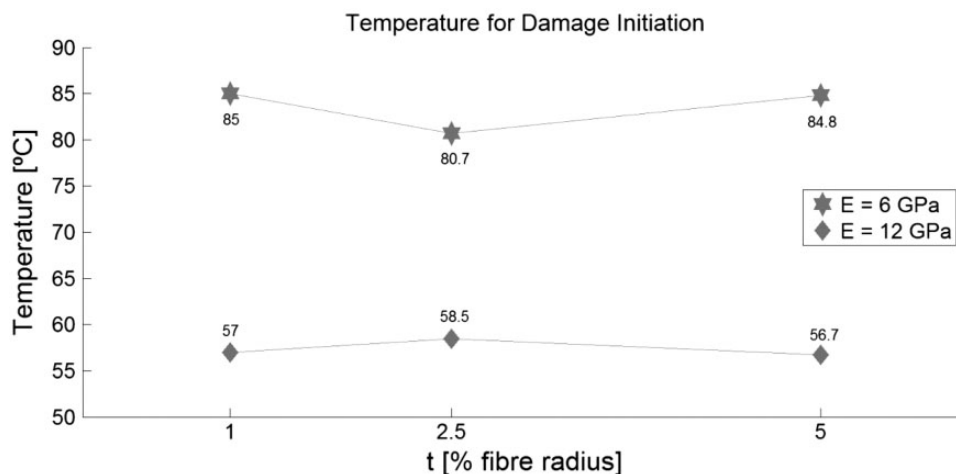


**Figure 7.** Temperature for damage initiation.

damage was detected in these cases. The stiffer the interphase, the lower the crack initiation temperature.

Damage initiation temperature is always in the range of 56–59°C in case of the interphase stiffness of 12 GPa, and always in the range of 80–85°C in case of 6 GPa.

With the interphase thickness of 2.5% of the fiber radius, the difference in damage initiation temperature—between cases of 6 GPa and 12 GPa—is 22.2°C. This difference amounts to 28°C and 28.1°C whether the interphase thicknesses are 1% and 5% of the fiber radius, respectively. This suggests that the thickness of the interphase does not have a significant influence on the initiation temperature.

On the other hand, as seen in Figure 8, the damage ratio parameter ( $\beta$ ) shows that a larger initial damage is reached in the 6 GPa interphase cells than in the 12 GPa ones (with an average value of damage ratio of 0.265 and 0.159, respectively). Figure 9 illustrates the cells status after the crack initiation step for the cases of study with  $E=6$  GPa and  $t=2.5\%$ , and  $E=12$  GPa and  $t=5\%$  (highest and lowest damage parameter calculated, respectively).

Focusing on the fatigue steps, the value of the interphase thickness appears to have a strong correlation with the crack propagation phase. Cells with an interphase thickness of 1% of the fiber radius develop microdamage as debondings in the small areas, which stabilize after a few cycles (in the order of 10–20 cycles) and do not propagate further. Cells with an interphase thickness of 2.5% and 5% develop large cracks, which propagate until the edge of the cell, or the surface of a contiguous fiber. As a general assumption, comparing the same values of the interphase thickness, the crack propagation is faster in a cell with a stiffer interphase. In neutral environment, in order to reach the

stabilization criteria, cracks require 88 cycles ( $t=2.5\%$ ), and 65 cycles ( $t=5\%$ ), whether the interphase stiffness ( $E$ ) is 12 GPa and, respectively, 115 and 120 cycles if  $E=6$  GPa.

Figure 10 shows a comparison between the equivalent displacement of the cell in different cases of the study, in oxidative and neutral environment.

Additionally, the percentage of variation of such value ( $\gamma$ ), for a unit cell simulated in the oxidative atmosphere ( $\delta u_{eq}^{ox}$ ) relative to the one in the neutral atmosphere ( $\delta u_{eq}^{in}$ ), is reported in Table 2. This variation is defined as follows

$$\gamma = \frac{\delta u_{eq}^{ox} - \delta u_{eq}^{in}}{\delta u_{eq}^{in}} \cdot 100 \quad (8)$$

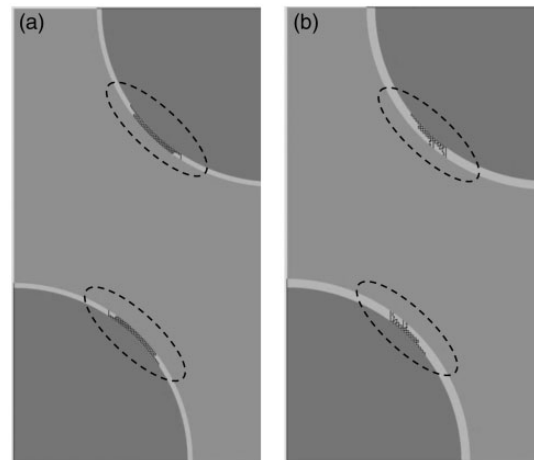


Figure 9. Damaged elements with interphase of: (a)  $E=6$  GPa,  $t=2.5\%$  and (b)  $E=12$  GPa,  $t=5\%$ .

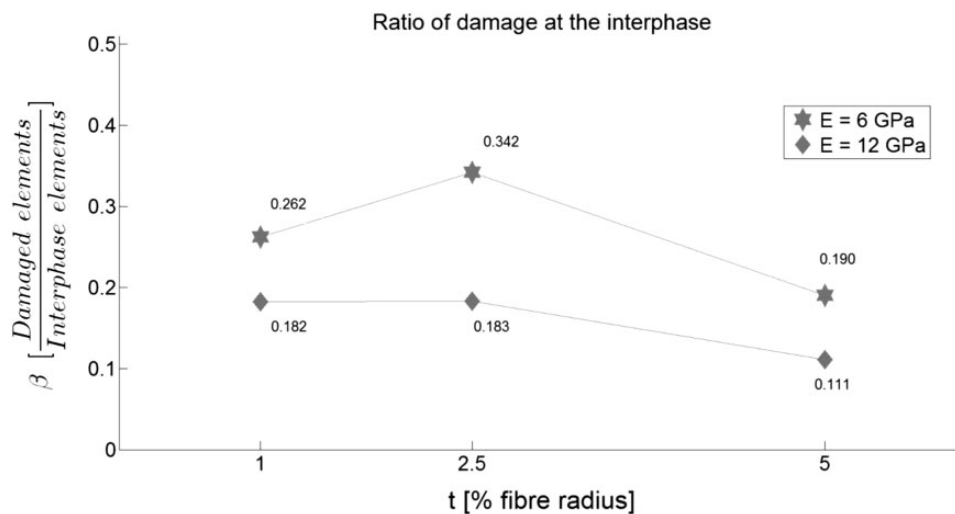


Figure 8. Damage parameter at the interphase.

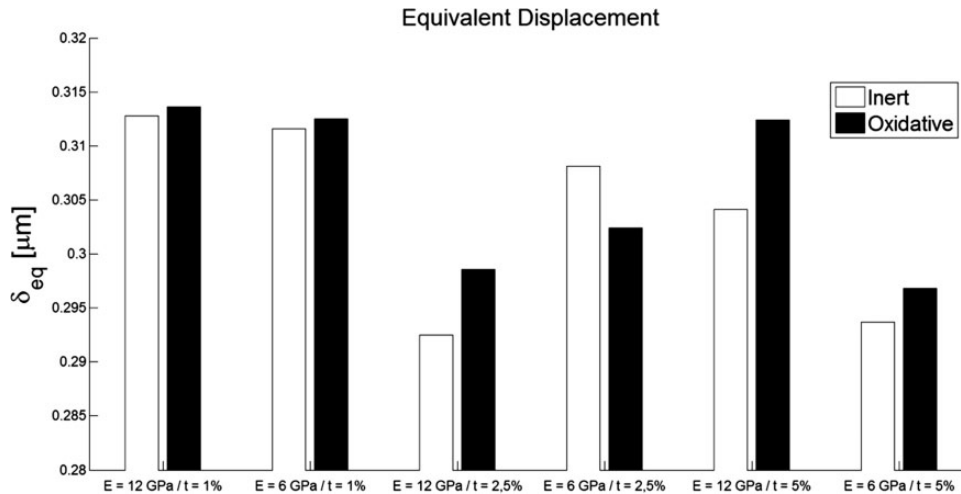


Figure 10. Equivalent displacement evaluated considering inert and oxidative atmosphere.

Table 2. Variation of  $\delta u_{eq}$  between oxidative and inert environment.

Combination of [E (GPa); t (%)]	$\gamma$ (%)
[12; 1]	0.256
[6; 1]	0.289
[12; 2.5]	2.085
[6; 2.5]	-1.850
[12; 5]	2.729
[6; 5]	1.055

The results suggest that a bigger damage is achieved in the oxidative environment. The very small variation in cases with  $t=1\%$  can be explained by the fact that the interphase debondings do not evolve as large matrix cracks, and the final damage is limited.

In the case of  $E=6$  GPa and  $t=2.5\%$ , the equivalent displacement shows a different behavior, being higher in the inert than in the oxidative atmosphere. This is assumed to be due to the different crack paths achieved in the two environments. In the neutral atmosphere, a large part of the matrix section gets encircled by two intersecting cracks (“A” and “B”, see Figure 11) and does not contribute to the overall cell stiffness. This crack behavior does not correspond with the real one, as is observed in the microscopic analysis.

Figures 12 and 13 show variation (in percentage) of the equivalent displacement parameter (or loss of stiffness) for each type of cell in the six cases of the study. It was calculated with respect to the equivalent displacement of a unit cell, with the same interphase parameters ( $E$  and  $t$ ), but without enriched elements activation for the simulation, and therefore without fatigue damage.

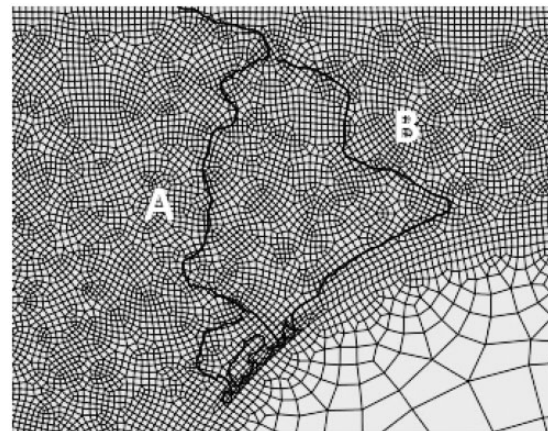


Figure 11. Detail of the cracks path in case of  $E=6$  GPa and  $t=2.5\%$ , in neutral environment.

Table 3 illustrates extreme cases, in terms of stiffness degradation, of the unit cells status after the simulation. The case of  $E=12$  GPa and  $t=5\%$ , which is the one showing the larger damaged area, shows the biggest difference in  $\delta u_{eq}$  values between neutral and oxidative environments (7.21% in oxidative, 4.38% in neutral).

The  $\delta u_{eq}$  variation values for cases with  $t=1\%$  are very close to each other, and always in the range of 3.81–4.38% for both interphase elastic moduli and environments. This could be explained by the fact that both unit cells reach a similar damage status (small debonding in the interphase region).

Case with parameters of  $E=6$  GPa and  $t=2.5\%$ , due to the aforementioned reasons, shows a different behavior from the general trend ( $\delta u_{eq}$  variation is 5.96% in neutral environment against 3.99% in the oxidative one).

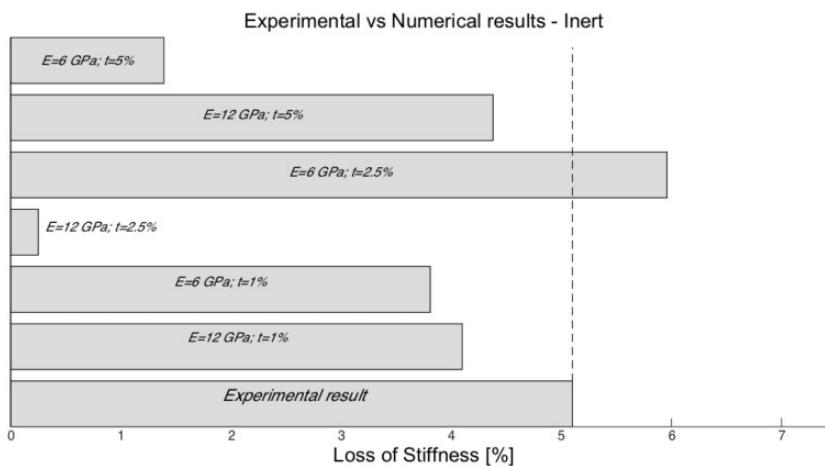


Figure 12. Equivalent displacement variation considering inert atmosphere.

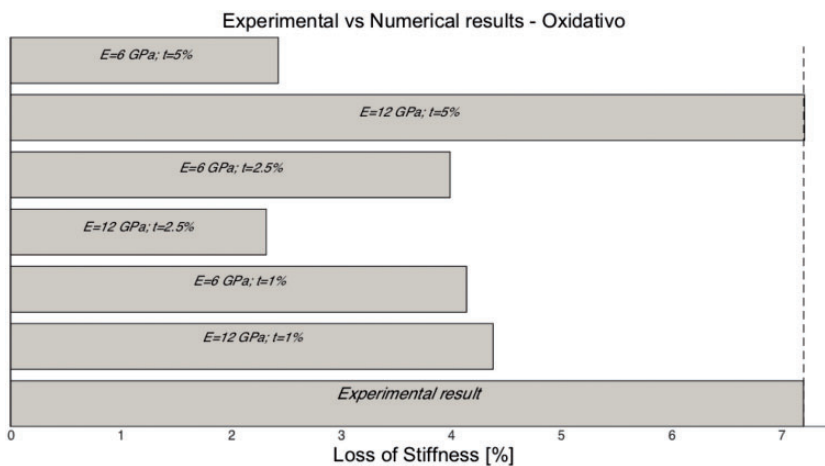
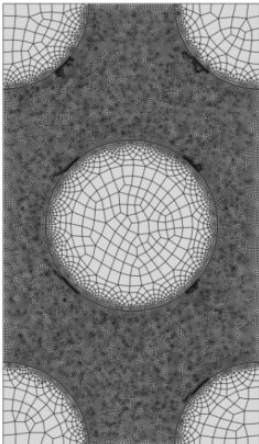
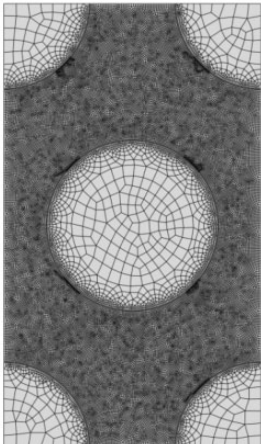


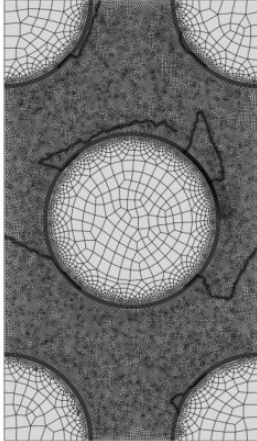
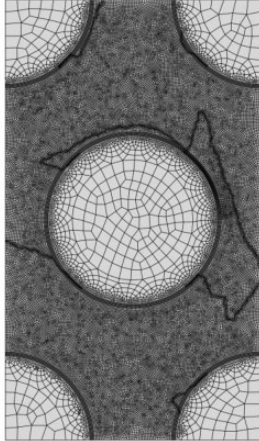
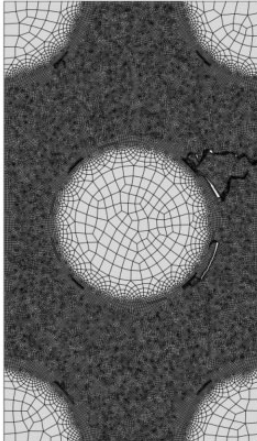
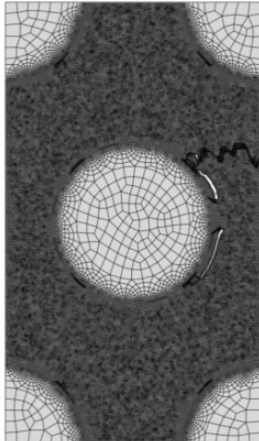
Figure 13. Equivalent displacement variation considering oxidative atmosphere.

Table 3. Cell status after thermal cycling simulation.

Model parameters	Inert atmosphere	Oxidative atmosphere
$E = 12 \text{ GPa} / t = 1\%$		

(continued)

**Table 3.** Continued

Model parameters	Inert atmosphere	Oxidative atmosphere
$E = 12 \text{ GPa} / t = 5\%$		
$E = 6 \text{ GPa} / t = 2.5\%$		

Experimental tensile test results are also showed and compared in terms of loss of stiffness. After 500 thermal cycles, a stiffness reduction of 7.1% and 5.2%, are reached in oxidative and inert atmosphere, respectively. Numerical results cannot be directly correlated with the experimental ones (effects such as different oriented layers or matrix shrinkage are not considered in this finite element study). However, it is possible to compare and observe that, at least for cases of  $E = 12 \text{ GPa}$ ,  $t = 5\%$ , and  $E = 6 \text{ GPa}$ ,  $t = 2.5\%$ , both results are in good agreement with the experimental ones. A significant variation of the measured Young's modulus between samples tested in oxidative and inert atmospheres is reflected by a significant variation of the equivalent displacement increase between the two cases.

## Conclusions

Several conclusions can be extracted from the presented study:

- (i) Extremely soft interphase acts as a “dumper”, reducing and homogenizing the stress field in the matrix; thus no crack initiation is observed in this kind of cells.
- (ii) Cracks appear in unit cells with an interphase stiffness of  $1/2$  and  $2/3$  of the fiber stiffness.
- (iii) In this study,  $T_g$  is assumed to be  $180^\circ\text{C}$ . Temperature for crack initiation is calculated below  $90^\circ\text{C}$  for all the considered cases in the first thermal cycle applied. Experimentally, crack initiation occurs within the first five cycles applied,

therefore, concentration of stresses due to the CTE mismatch, and not the matrix oxidation, may have caused the crack initiations.

- (iv) Thicker and stiffer interphase promotes a lower crack initiation temperature and a faster crack dynamic.
- (v) The damage level observed after 500 cycles in the oxidative environment is higher than the one observed after 500 cycles in the inert environment.

Comparison of the experimental and numerical tests, in terms of loss of stiffness, suggests that the most realistic couple of interphase parameters is  $E = 12$  GPa and  $t = 5\%$  for both inert and oxidative atmosphere (disregarding the case with  $E = 6$  GPa and  $t = 2.5\%$ , due to the unrealistic path of cracks).

Finally, for future developments and more thorough comparisons between the experimental tests and the numerical simulations, additional research should be focused on:

- (a) Incorporation of time-dependent matrix and interphase strength reduction (due to the oxidation reactions). Experimental work should be performed on thin sheets of Hexcel<sup>®</sup> 8552 resin (i.e. tensile testing according to the ASTM D882 “Standard Test Method for Tensile Properties of Thin Plastic Sheetings”); and on matrix–fiber bonding interphase at different levels of oxidation.
- (b) Developing a 3D model of unit cells, including shrinkage effects caused by matrix oxidation, which induce additional local stresses on both matrix and interphase.<sup>35,36</sup>
- (c) Following the step (b), developing a meso-scale model to implement the effect of the CTE mismatch among the layers of different orientation. Detailed XFEM 3D model of the plies would be too computationally expensive, and a procedure of homogenization of the layer properties evolution with the aging time should therefore be applied (i.e. through field variable functions).

#### Declaration of Conflicting Interests

The author(s) declared no potential conflicts of interest with respect to the research, authorship, and/or publication of this article.

#### Funding

The author(s) received no financial support for the research, authorship, and/or publication of this article.

#### References

1. Gay D and Hoa Suong V. *Composite materials: Design and applications*, 2nd ed. Paris: CRC Press Taylor & Francis Group, 2007.
2. Barbero Ever J. *Finite element analysis of composite materials using Abaqus*. Bosa Roca: CRC Press Taylor & Francis Group, 2013.
3. Talreja R. *Damage mechanics of composite materials*. Amsterdam: Elsevier, 1994.
4. Gigliotti M, Minervino M and Lafarie-Frenot MC. Assessment of thermo-oxidative induced chemical strain by inverse analysis of shrinkage profiles in unidirectional composites. *Compos Struct* 2016; 157: 320–336.
5. Gigliotti M, Minervino M, Lafarie-Frenot MC, et al. Effect of thermo-oxidation on the local mechanical behaviour of epoxy polymer materials for high temperature applications. *Mech Mater* 2016; 101: 118–135.
6. Flore D, Wegener K, Seel D, et al. Investigation of chemical ageing and its effect on static and fatigue strength of continuous fibre reinforced plastics. *Compos Part A: Appl Sci Manuf* 2016; 90: 359–370.
7. Ghasemi AR and Moradi M. Effect of thermal cycling and open-hole size on mechanical properties of polymer matrix composites. *Polym Test* 2017; 59: 20–28.
8. Ghasemi AR and Moradi M. Failure analysis of the NOL-ring polymer matrix composites under thermal cycling. *Polym Compos* 2017.
9. Ghasemi AR and Moradi M. Low thermal cycling effects on mechanical properties of laminated composite materials. *Mech Mater* 2016; 96: 126–137.
10. Zhang C, Binienda WK, Morscher GN, et al. Experimental and FEM study of thermal cycling induced microcracking in carbon/epoxy triaxial braided composites. *Compos Part A: Appl Sci Manuf* 2013; 46: 34–44.
11. Moure MM, Garcia-Castillo SK, Sánchez-Sáez S, et al. Matrix cracking evolution in open-hole laminates subjected to thermo-mechanical loads. *Compos Struct* 2017.
12. Mathilde J, Marie-Laure D and Marie-Josée P. Study of damage induced by extreme thermal cycling in cyanate ester laminates and sandwich panels. *J Compos Mater* 2017; 51: 2023–2034.
13. Rouquie S, Lafarie-Frenot MC, Cinquin J, et al. Thermal cycling of carbon/epoxy laminates in neutral and oxidative environments. *Compos Sci Technol* 2005; 65: 403–409.
14. Lafarie-Frenot MC and Ho NQ. Influence of free edge intralaminar stresses on damage process in CFRP laminates under thermal cycling conditions. *Compos Sci Technol* 2006; 66: 1354–1365.
15. Lafarie-Frenot MC, Rouquie S, Ho NQ, et al. Comparison of damage development in C/epoxy laminates during isothermal ageing or thermal cycling. *Compos Part A: Appl Sci Manuf* 2006; 37: 662–671.
16. Olivier L, Ho NQ, Grandidier JC, et al. Characterization by ultra-micro indentation of an oxidized epoxy polymer: Correlation with the predictions of a kinetic model of oxidation. *Polym Degrad Stab* 2008; 93: 489–497.

17. Decelle J, Huet N and Bellenger V. Oxidation induced shrinkage for thermally aged epoxy networks. *Polym Degrad Stab* 2003; 81: 239–248.
18. Paris F, Cañas J, Marín JC, et al. *Introduction to the design and analysis with composites materials*. Seville: University of Seville, 2012.
19. Brodowsky HM, Jenschke W and Mäder E. Characterization of interphase properties: Microfatigue of single fibre model composites. *Compos Part A: Appl Sci Manuf* 2010; 41: 1579–1586.
20. Asp LE, Berglund LA and Talreja R. Effects of fibre and Interphase on matrix initiated transverse failure in polymer composites. *Compos Sci Technol* 1996; 56: 657–665.
21. Maligno AR, Warrior NA and Long AC. Effects of interphase material properties in unidirectional fibre reinforced composites. *Compos Sci Technol* 2010; 70: 36–44.
22. Tanoglu M, McKnight SH, Palmese GR, et al. Effects of glass-fibre sizing on the strength and energy absorption of the fibre/matrix interphase under high loading rates. *Compos Sci Technol* 2001; 61: 205–220.
23. Foley ME, Abu Obaida A, Huanga X, et al. Fibre/matrix interphase characterization using the dynamic interphase loading apparatus. *Compos Part A: Appl Sci Manuf* 2002; 33: 1345–1348.
24. Jina CF, Zhub QZ and Shaoa JF. A numerical analysis of interface damage effect on mechanical properties of composite materials. *Mech Res Commun* 2014; 62: 18–24.
25. Este A, Toson B, Saliba J, et al. A new approach to simulate interface damage in brittle matrix composites. *Procedia Struct Integr* 2016; 2: 2456–2462.
26. Hyer MW and Waas AM. *Comprehensive composite materials*. Oxford: Elsevier, 2000, Vol. 1, pp.345–375.
27. Cowin SC and Mehrabad M. Anisotropic symmetries of linear elasticity. *Appl Mech Rev* 1995; 48: 247–285.
28. Zhang Y, Xia Z and Ellyin F. Evolution and influence of residual stresses/strains of fibre reinforced laminates. *Compos Sci Technol* 2004; 64: 1613–1621.
29. Li S. Boundary conditions for unit cells from periodic microstructures and their implications. *Compos Sci Technol* 2008; 68: 1962–1974.
30. Belytschko T, Gracie R and Ventura G. A review of extended/generalized finite element methods for material modeling. *Model Simul Mater Sci Eng* 2009; 17: 1–24.
31. Grogan DM, Ó Brádaigh CM and Leen SB. A combined XFEM and cohesive zone model for composite laminate micro-cracking and permeability. *Compos Struct* 2015; 120: 246–261.
32. Liu H-Y, Wang GT and Mai YW. Cyclic fatigue crack propagation of nanoparticle modified epoxy. *Compos Sci Technol* 2012; 72: 1530–1538.
33. Olivier L, Baudet C, Bertheau D, et al. Development of experimental, theoretical and numerical tools for studying thermo-oxidation of CFRP composites. *Compos Part A: Appl Sci Manuf* 2009; 40: 1008–1016.
34. Lafarie-Frenot MC, Rouquie S, Ho NQ, et al. Comparison of damage development in C/epoxy laminates during isothermal ageing or thermal cycling. *Compos Part A: Appl Sci Manuf* 2006; 37: 662–671.
35. Gigliotti M, Olivier L, Quy Vu D, et al. Local shrinkage and stress induced by thermo-oxidation in composite materials at high temperatures. *J Mech Phys Solids* 2011; 59: 696–712.
36. Olivier L, Baudet C, Bertheau D, et al. Development of experimental, theoretical and numerical tools for studying thermo-oxidation of CFRP composites. *Compos Part A: Appl Sci Manuf* 2009; 40: 1008–1016.